

Article

An Alternative Parallel Mechanism for Horizontal Positioning of a Nozzle in an FDM 3D Printer

Edoardo Idà ^{1,*}, Federico Nanetti ² and Giovanni Mottola ³

¹ Department of Industrial Engineering, University of Bologna, 40126 Bologna, Italy

² Mark One Srl, 47025 Cesena, Italy; tecnico@3dmarkone.com

³ Department of Sciences and Methods for Engineering, University of Modena and Reggio Emilia, 42122 Reggio Emilia, Italy; giovanni.mottola@unimore.it

* Correspondence: edoardo.ida2@unibo.it

Abstract: In 3D printer design, special care must be taken when choosing the print head positioning mechanism. Indeed, this choice has a significant influence on the manufacturing accuracy, printing speed, workspace characteristics, and total cost of the printer. Considering 3D printers with layer-based processes, many designs include two stages: a planar mechanism for positioning the nozzle on a horizontal plane and a linear mechanism for the vertical build-plate motion. From the literature, two designs are usually applied for horizontal motion, commercially known as “CoreXY” and “H-bot”. Their load distribution characteristics are compared here: it is found that both have significant drawbacks. Therefore, an alternative architecture, called “CoreH-bot,” is introduced to overcome such limitations; this mechanism is both fully planar, which greatly simplifies its design and assembly phases while increasing part life, and has low unbalanced torques during motion, which increases the maximum speed for the given accuracy. The CoreH-bot kinematic equations are analyzed to define the Jacobian matrix and the corresponding workspace. The static and dynamic analyses are also performed. A prototype with this architecture has been designed that shows interesting capabilities in terms of print speed, while being both simple and cost-effective to assemble.



Citation: Idà, E.; Nanetti, F.; Mottola, G. An Alternative Parallel Mechanism for Horizontal Positioning of a Nozzle in an FDM 3D Printer. *Machines* **2022**, *10*, 542. <https://doi.org/10.3390/machines10070542>

Academic Editor: Marco Ceccarelli

Received: 30 May 2022

Accepted: 27 June 2022

Published: 4 July 2022

Publisher’s Note: MDPI stays neutral with regard to jurisdictional claims in published maps and institutional affiliations.



Copyright: © 2022 by the authors. Licensee MDPI, Basel, Switzerland. This article is an open access article distributed under the terms and conditions of the Creative Commons Attribution (CC BY) license (<https://creativecommons.org/licenses/by/4.0/>).

1. Introduction

1.1. Architectures for 3D Printing

Within the larger field of rapid prototyping, *additive manufacturing* (AM) is now one of the leading technologies [1,2]. This concept was first introduced in the 1980s [3,4] to quickly produce presentation models cost-effectively. In AM, a flow of material is deposited, usually by layers, to obtain the desired shape [5]; this process allows designers to produce shapes that would be impossible (or impractically expensive) to manufacture through conventional machining methods (which are generally *subtractive*, meaning that material is removed to obtain a shape). For these reasons, AM has attracted strong interest both in industrial and academic settings and has found applications in several fields requiring high levels of customization, such as architectural models, medical implants, molds for investment casting, artistic products, and components for the aerospace industry and spare parts manufacturing [1,2,6–8].

Out of the many technologies for AM, *3D printing*, in particular, has seen an explosive growth in recent decades, also due to the expiration of early patents [7,9,10] that restricted the development of core technologies; recent analyses report a 320% market growth in the 2015–2020 period [11], while 3D printing has also been proposed for very large elements, including entire buildings. We focus here on desktop devices: these commonly employ thermoplastics, such as acrylonitrile butadiene styrene (ABS), polylactic acid (PLA), polyamide (PA), and Nylon [8,12,13]. The plastic is heated slightly above its melting point

and deposited by a print head on a plate; this process, called *Fused Deposition Modeling* (FDM), is currently used in 48% of 3D printers [8,11] as it is robust, simple, intrinsically scalable and highly versatile in terms of the materials that can be employed [10,14]. Commonly, FDM printers use a plastic filament fed through a heated nozzle (Figure 1a); this method, called *Fused Filament Fabrication* (FFF), is predominant in FDM applications [12], to the point that FDM and FFF are often used as equivalent definitions.

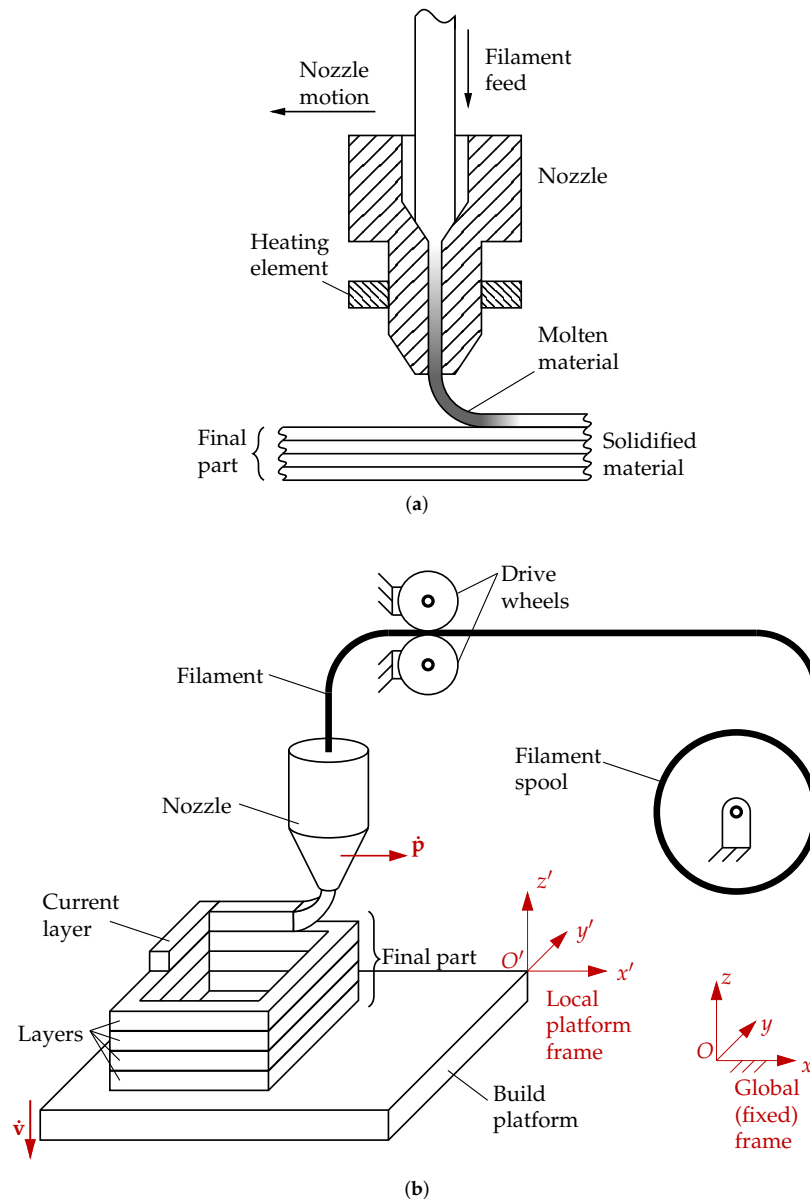


Figure 1. (a): Schematic of material deposition nozzle for FFF processes. (b): Schematic of an FFF device with Cartesian XY head architecture. The velocity \dot{p} of the nozzle is in the horizontal ($x-y$) plane, while the vertical motion \dot{v} is directly provided to the build platform on which the part is formed.

In FDM, the nozzle depositing the molten plastic has to move with respect to a build platform, on which the part is progressively formed (layer by layer) as the plastic resolidifies, as illustrated in Figure 1b. Thus, a motion system is required; this system has to carry the nozzle at high velocity to improve print speeds, while maintaining high accuracy. Several mechanisms have been proposed for moving the nozzle in FDM printers; some common architectures are described in the following. We mainly focus on 3-Degree-of-

Freedom (3-DoF) mechanisms in which the relative orientation of the nozzle with respect to the platform is constant, since these are very common in practical applications.

- (a) *Cartesian* mechanisms control the three components of the nozzle velocity (with respect to the build platform) along three coordinate axes independently; this greatly simplifies the kinematic analysis. Usually, the build platform has one DoF along one axis, while the nozzle has two DoFs along the other two axes. This is the most common architecture in desktop FDM printers [3,9,10,15–21].
- (b) *Delta* printers use the parallel kinematic architecture of the Delta robot, proposed by R. Clavel; in particular, the *linear* version of the Delta is used, where prismatic pairs actuate the mechanism [22]. With this architecture, the nozzle's *end-effector* (EE) has only three translational DoFs, while the orientational DoFs are constrained. The main advantage is the fully parallel architecture, where the motors are fixed on the frame, which reduces the actuator torques. Moreover, the accuracy does not depend on the layer's height above the build platform; thus, Delta printers are suited for printing parts that develop mostly along a vertical direction. On the other hand, their kinematics are more complex than those of Cartesian architectures; also, Delta printers have a smaller workspace with respect to the footprint.
- (c) *SCARA* printers use a robot arm with one translational and two rotational joints to move the nozzle [23]; the concept is derived from SCARA robots used in production lines [24]. While SCARA printers can provide a larger workspace than Delta printers, they are less rigid (and thus less accurate) due to their serial architecture.
- (d) *Polar* printers rotate the platform around a fixed axis, while the nozzle usually has two translational DoFs, along the vertical and the radial directions [25]. This design is cost-effective and leads to smaller footprints; however, the 3D printed part moves as the platform rotates, inducing vibrations that reduce the print accuracy.
- (e) *Anthropomorphic* architectures use a conventional serial arm, such as those of industrial robots used in production lines; unlike SCARA systems (type c), these generally have more than three DoFs. These mechanisms, thus, have greater freedom of motion and can realize more complex parts, but the issues related to the stiffness and the inertial effects of the serial architecture are even more pressing in this case e [26].

For comparison, Cartesian and Delta commercial printers in the medium-high price range can achieve speeds up to $80 \frac{\text{mm}}{\text{s}}$ while maintaining the print quality of the components. This is one of the main advantages of these designs, as the top speeds for comparable devices with designs of types c to e are much lower.

While previous works have considered the effects of the material properties [12] or the control system [17] on the final accuracy, we focus instead on improvements of the motion architecture. We considered a Cartesian architecture (type a). These are generally inexpensive to build and simple to design and assemble; moreover, machines with this architecture are generally fast and accurate, which are essential requirements for practical use. We also aim to achieve a workspace comparable to the printers available on the market while minimizing the footprint. Our design employs a system of pulleys and synchronous belts; this is an approach used in several desktop printers, which leads to an inexpensive design and a lightweight mechanism. In particular, the design presented here improves other previous alternatives in terms of compactness and accuracy; as it will be seen, our design combines the advantages of the two Cartesian architectures most commonly used, as it reduces the unbalanced torques during motion (as in the CoreXY), while also keeping the belt routing entirely within the same plane (as in the H-bot), which is desirable for design simplicity. We also show how a large workspace can be achieved while maintaining a high stiffness and a fully-parallel architecture (with all motors fixed on the frame), which significantly reduces the moving masses and allows us to achieve high print speeds.

The rest of this work is organized as follows: In the next Section 2.2, we discuss the main design alternatives for FDM printers with Cartesian architectures and their advantages and shortcomings. We also introduce the *CoreH-bot* architecture, an alternative pulley-and-belt routing for moving the nozzle in a plane. The kinematic analysis of the *CoreH-bot* is

in Section 2, in which we derive the Jacobian matrix for the mechanism and analyze its workspace. In Section 3, we compare the different belt routings, studying their behavior both under static and dynamic conditions, and consider the force transmission between the actuated pulleys and the EE. We also show that our design significantly reduces the unbalanced torques on the EE, thus, improving the printing accuracy. The prototype of the printer that we developed and the results from preliminary tests are presented in Section 4. Finally, in Section 5, we summarize our conclusions and suggest directions for future work.

1.2. Kinematics for 3D Printers

Firstly, we introduce coordinate frames to define the relative motion of the nozzle with respect to the build platform. A coordinate frame $\mathcal{F}' = (O', x', y', z')$, called the *machine coordinate system* [5], is defined on the platform (Figure 1b); since the platform (and, thus, the frame \mathcal{F}') is mobile in some architectures, it is also convenient to define a (fixed) *global* coordinate frame $\mathcal{F} = (O, x, y, z)$. Note that here and in the following, a prime symbol denotes vectors defined in the machine frame \mathcal{F}' ; the z axis is vertical (normal to the layers), while the x axis is parallel to the front of the machine [5].

While the material is deposited on the platform, the velocity $\dot{\mathbf{p}}$ of the nozzle is on a horizontal plane. Usually, the z -axis motion, which requires precise movements at relatively low speeds, is provided by a lead screw actuator; the motion on the horizontal plane can instead be obtained by flexible elements such as cables or belts to increase the workspace.

Within the general Cartesian printer concept (type a), there is significant design flexibility; several implementations have been proposed in commercially available printers, which have relevant differences in terms of speed, accuracy, and footprint.

Broadly speaking, two architectures can be found in most prototypes. Both architectures have a mechanism for moving the nozzle along two coordinate axes, while the remaining DoF corresponds to the platform motion. The architectures are described below.

(a.1) *XZ head* printers (Figure 2a) have a frame with two vertical guides, along which a horizontal bar moves (along the z axis); on the said horizontal bar, the nozzle moves along the x axis. The motion along the y axis is applied to the platform instead. This is the most straightforward architecture, commonly employed in low-end printers for hobbyists. The main drawback is that increasing the print speed implies increasing the platform velocity (along the y axis), leading to rapid motions of the part being built, thus, inducing vibrations and lowering the accuracy. Moreover, the x -axis motor is attached to the horizontal bar, thus, increasing the moving mass.

(a.2) In *XY head* printers (Figure 2b), the platform performs only motions along the z axis, which are much slower than those on the layer plane; thus, the accuracy is significantly increased. Furthermore, the workspace projection in the layer plane almost coincides with the footprint, which is, thus, smaller with respect to *XZ head* printers. This architecture is typical in high-end printers for professional use; while faster and more accurate, *XY head* printers are also more complex to design, and thus, more expensive.

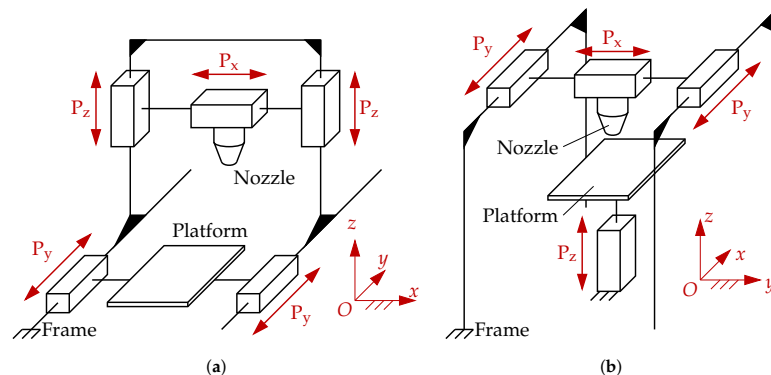


Figure 2. (a): Schematic of a printer with Cartesian XZ head architecture. (b): The same for XY head. The rectangular cuboids are prismatic (P) joints, where the subscript (x , y , or z) denotes the motion axis.

We then consider an XY head printer and focus on the mechanism for the motion on the horizontal plane; all designs studied here have a bar aligned with the x axis, along which the nozzle moves, while the bar itself moves along the y axis on lateral guides.

The design alternatives found in the literature for type a.2 are described below.

- (a.2.i) A *serial* mechanism moves the nozzle along the y axis with motors fixed on the frame, while the motion along x is provided by a motor that is fixed on the bar. While this design is quite simple, the mass of the motor on the bar significantly increases the moving masses; thus, this option is seldom used [3,9,10].
- (a.2.ii) A *stacked* mechanism uses two stages: in each stage, the motor is fixed and causes a bar to move along guides. The stages are stacked on top of each other, with the second being rotated by 90° (along the z axis) with respect to the first. The nozzle is connected to both bars and can, thus, move on the $x-y$ plane, its position being defined by the intersection of the two bars. While this approach reduces the moving masses, it significantly increases the printer size in the vertical direction and leads to a more complex design.
- (a.2.iii) A *parallel* mechanism usually has frame-fixed actuators; a parallel kinematic chain connects the motors to the nozzle. Often, a flexible element is used to transmit the movement; then, the bar and the lateral guides serve only to constrain the motion, which remains purely translational (on the horizontal plane).

The use of flexible elements, such as synchronous belts, to transmit motion from frame-fixed motors to an EE having purely translational motion (type a.2.iii) is, in fact, a common solution that is not limited to 3D printers. For instance, similar concepts have been applied to gait simulators [27,28], rehabilitation devices [29], robots for assistive lifting [30], and pick-and-place systems [31–34]. These systems are easy to design, transport and assemble, while also providing large workspaces and high payload-to-total-weight ratios.

Most previous works use either one of two variations of the type a.2.iii design, commonly called *H-bot* and *CoreXY*; we briefly summarize them in the following Sections 1.2.1 and 1.2.2, and then introduce our alternative concept in Section 2.

From now on, we assume that the flexible elements are synchronous belts unless otherwise specified; this way, the motion is transmitted accurately from the motors to the mechanism, without slippage between the belts and the pulleys. For this reason, practical designs for FDM printers [9,16,20] almost exclusively employ belts. Some works [35–37] on mechanisms with flexible elements for translational motion consider using cables instead, as cables can be routed freely in space. Otherwise, non-planar routings require twisting the belts, increasing stresses and reducing their useful life. Since we consider mechanisms that are strictly contained in a plane, using belts is not a limitation in our case.

1.2.1. H-Bot

“H-bot” is the common name of the schematic in Figure 3, with a belt routed in a figure-H pattern. Four pulleys are frame-fixed, and two of these are actuated. The other (mobile) pulleys are connected to a bar, moving along the y axis (on two lateral guides). This design uses a one-sided synchronous belt: the teeth are inside the belt loop, thus, the fixed pulleys are toothed, while the mobile ones are smooth, as they touch the belt only on the outside.

The design in Figure 3 is not unique, as other pulleys could be actuated. However, two actuated pulleys cannot be both directly connected by a belt segment and attached to the same rigid body; otherwise, their rotations are not independent, since the belt is considered to be inextensible (this condition also applies to the other routings). This design uses one open belt, of which the ends are attached to the print head (the rounded rectangle in Figure 3). The velocity of the print head depends on the speeds ω_1 and ω_4 of the two motors. For instance, if $\omega_1 = \omega_4$ (with the directions in Figure 3), then the print head will move along the x axis.

This design is compact, contained in the $x-y$ plane, and has reduced moving masses. Thus, it has been used in several FDM printers [10,15,17–19,21]. This concept is, in fact, older

than FDM printing and can be found in several mechanisms that move objects in a plane. For instance, routings that are conceptually equivalent to the one in Figure 3 have been proposed for recording devices [38], positioning systems [34,39,40], X-ray scanners [41,42], laser cutters [43] and load-hoisting gantries [35,44,45]. The H-bot lends itself to modular designs, in which two routings are combined to obtain more complex (4-DoF) motions [46,47]. The long belt induces low stiffness and high vibrations, however, and the H-bot is unbalanced during motion (Section 3); the belt applies a torque on the bar, causing a racking effect [17,21].

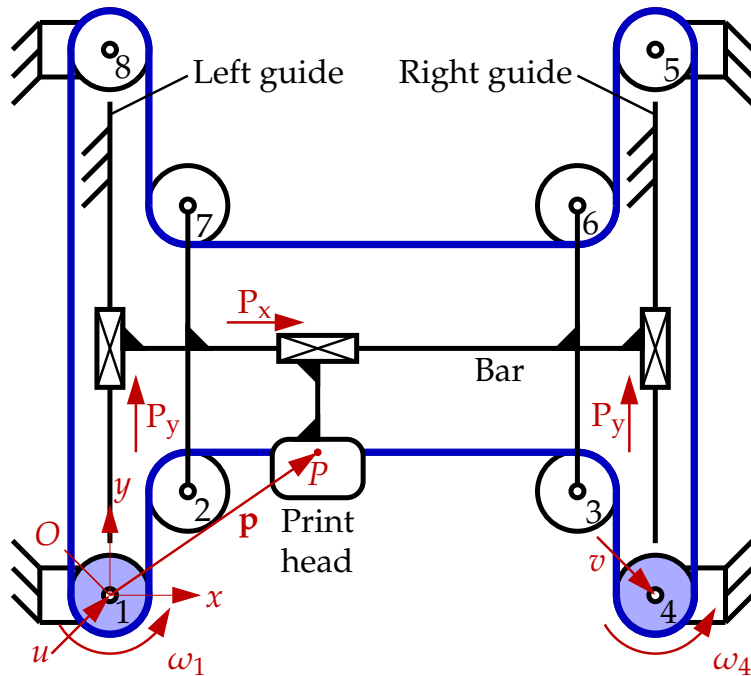


Figure 3. Schematic of an H-bot routing (as seen from the top of the printer). The pulleys connected to the motors (1 and 4) are colored, while the other pulleys are in white; the belt that wraps around the pulleys is in blue. The rectangles denote P joints, while the small circles correspond to R joints.

1.2.2. CoreXY

In the CoreXY design, two open belts (Figure 4) are actuated by two motors and attached to the print head at their ends; the head velocity is a linear combination of ω_1 and ω_4 .

The CoreXY is *partially balanced*, as lower torques are applied to the bar during motion. Thus, this design has lower vibrations and higher accuracy than the H-bot, also because shorter, stiffer belts are used; thus, higher speeds can be reached for a given mass of the print head. Moreover, the footprint is relatively small and comparable to the H-bot.

This design, first introduced for a portable printer [20] (an earlier concept, with one half of the routing, for 1-DoF motion, is in [35]) has attracted significant interest [10,16,21] and has been proposed for other applications, such as medical devices [48].

This design, however, requires two more pulleys than the H-bot and is not planar, as the belts overlap. Since the belts cannot cross, there are two design options, as follows:

- Twist the overlapping segments (Figure 4) along the lengths so that they rotate around each other without crossing. This approach increases the belt stress and reduces the useful life; also, preventing the belt segments from touching each other is complex.
- Place the belts on parallel planes. This complicates the assembly and increases the printer volume; also, greater bending torques may be applied on the motor shaft.

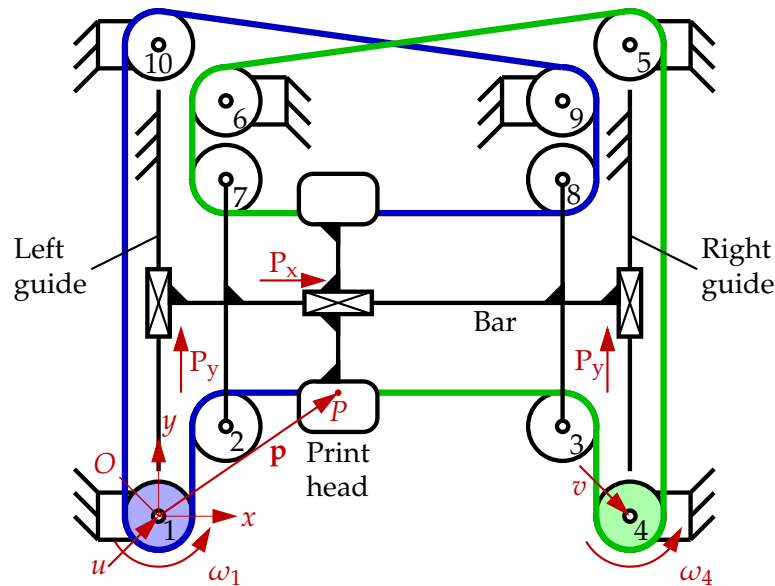


Figure 4. Schematic of a CoreXY routing (top view). For clarity, the two belts are colored; each actuated pulley has the color of the corresponding belt (again, pulleys 1 and 4 are actuated).

2. CoreH-Bot: Introduction and Kinematic Analysis

2.1. Introduction to the CoreH-Bot

Given the limitations of both the H-bot and the CoreXY concepts, as outlined previously, we propose an alternative routing, the schematic of which is reported in Figure 5. Unlike the CoreXY, this mechanism is fully planar, meaning that no belt segments overlap; this simplifies both the design and the assembly. Furthermore, the mechanism is partially balanced (like the CoreXY); this reduces the torque applied to the bar during the motion of the print head.

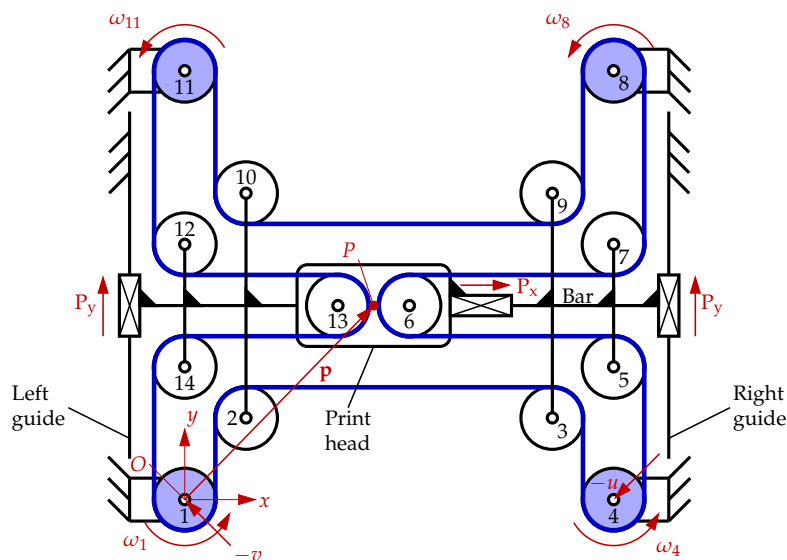


Figure 5. Schematic of a CoreH-bot (top view). Only one belt is used, as in the H-bot; the four actuated pulleys are colored. The coordinate frame $\mathcal{F} = (O, x, y, z)$ has origin at the center of pulley 1 (on the lower left); the pulleys are numbered, counting along the belt, in the counterclockwise direction.

Unlike both the CoreXY and the H-bot, this is a *closed-loop* design. Thus, the mechanism has 3 DoFs: two translations of the print head (along the x and y axes) and one DoF corresponding to the idle rotation of the belt over the pulleys (while the print head position

remains constant). At least *three* motors are then required; however, the belt rotation is an *internal* DoF, of which the control is not required for the printing process. *Four* motors are used instead for the control, each connected to one of the fixed pulleys (1, 4, 8, and 11); these motors are pairwise coupled, such that $\omega_1 = -\omega_8$ and $\omega_4 = -\omega_{11}$. Two independent rotations, thus, control the two DoFs of the print head; this way, the print head velocity is again a linear combination of the ω_i 's, and the control system is still as simple as the ones for the CoreXY and H-bot.

Since four motors control two DoFs, the mechanism is *overconstrained*. Admittedly, this may complicate the design, which also has four more pulleys than the CoreXY. However, we find that the improvements in both speed and accuracy more than compensate for the (possible) increase in cost, which is justified in a high-end printer that we developed for making prototypes with strict tolerances. Furthermore, due to symmetry, fewer custom-made parts are used than in the other designs; the Bill of Materials is thus shorter, which is desirable in large-scale production to contain costs. The CoreH-bot uses a longer belt than the H-bot, which could reduce the stiffness (and thus, the accuracy) in experimental tests. However, this issue was not found to be of serious concern (see Section 4).

We note that a conceptually similar design has been proposed among several others in a previous work [35] for a different application (a gantry crane). However, that design had three DoFs (including a rotation around the vertical axis), which are not required here; moreover, the authors did not explore the advantages of overconstraining the mechanism.

2.2. Kinematic Analysis

To define the print head position, we first take a reference point P on the head and define $\mathbf{p} = P - O = [x, y]^T$; then, for a given motion of the print head, we denote the components of the displacement $\Delta\mathbf{p}$ of P across the x and y axes as Δx and Δy , respectively. We also define the angular displacement $\Delta\theta_i$ of the i -th pulley as it rotates during said motion, while r_i is its radius. Here and in the rest of this work, the angular displacements $\Delta\theta_i$ are positive in the counterclockwise direction.

The kinematic analysis of the H-bot and the CoreXY is known from [20,39]; assuming that $r_i = r$ for all i , it was found that, for both architectures, it holds

$$\Delta\mathbf{p} = \begin{bmatrix} \Delta x \\ \Delta y \end{bmatrix} = r\mathbf{J}\Delta\theta, \quad \mathbf{J} = \frac{1}{2} \begin{bmatrix} 1 & 1 \\ 1 & -1 \end{bmatrix}, \quad \Delta\theta = \begin{bmatrix} \Delta\theta_1 \\ \Delta\theta_4 \end{bmatrix}. \quad (1)$$

Equation (1) defines the *direct* position kinematics of the H-bot and CoreXY routings; the *inverse* kinematics equation is obtained by inverting Equation (1), giving $\Delta\theta = \frac{1}{r}\mathbf{J}^{-1}\Delta\mathbf{p}$.

Considering infinitesimal displacements $d\theta = [d\theta_1, d\theta_4]^T$ over a time interval dt in Equation (1) and defining $\omega_i = d\theta_i/dt$, we obtain the direct *velocity* kinematics equation as

$$\dot{\mathbf{p}} = \frac{d\mathbf{p}}{dt} = r\mathbf{J} \frac{d\theta}{dt} = r\mathbf{J}\boldsymbol{\omega}, \quad \boldsymbol{\omega} = \begin{bmatrix} \omega_1 \\ \omega_4 \end{bmatrix} \quad (2)$$

(notice that the pulley radius r and the matrix \mathbf{J} are constant and do not depend on t). Matrix \mathbf{J} , thus, corresponds to the *direct kinematics Jacobian* of the H-bot and CoreXY routings. As observed in Section 1.2, we, thus, find that the print head motion is given by a linear combination of the motor speeds ω_1 and ω_4 . In particular, ω_1 and ω_4 are proportional to the print head velocity components along axes u and v , respectively (see again Figures 3 and 4).

The kinematic analysis of the CoreH-bot routing is more complex. Therefore, we apply the method for analyzing the complex pulley systems presented in [37], since it systematically allows us to obtain the kinematic equations. At the same time, the cited work considers cables as flexible elements for motion transmission, and the results can also be directly applied to belts. The essential hypotheses for applying the method in [37] are as follows:

- (I) all belt segments have constant orientation, along either the x - or the y -axis;

- (II) elastic deflections are disregarded and the belt length is the same under tension;
- (III) the belt is always in tension (that is, it does not become slack). This is achieved by a specific design (see Section 4), such that the tension is maintained during motion;
- (IV) the belt wraps on pulleys, and no slippage occurs between the belt and the pulleys;
- (V) the pulleys are connected by R joints to rigid blocks, either fixed or translating along one (or both) of the coordinate axes (with fixed orientation).

Indeed, these hypotheses are applicable here without significantly restricting the analysis. An essential advantage of this method is that it allows us to consider general routings without any assumptions on the pulley radii nor on the relative positions of the pulleys with respect to the blocks on which they are attached; we do assume, however, that the pulley radii and their relative positions are chosen such that each belt segment is parallel to one of the coordinate axes at an initial reference position, so that condition I is satisfied.

In our case, we have 14 pulleys (numbered as in Figure 5); we denote the center of the i -th pulley as point P_i . We also define 14 belt nodes, one on each belt segment: belt node N_i is a point on the segment between pulleys i and $i + 1$. The positions of the N_i 's are not indicated in Figure 5, as they can be freely chosen at any point on the corresponding belt segment without changing the results of the analysis. Finally, we define blocks 1, 2, and 3, corresponding to the fixed frame, the bar, and the print head, respectively; their positions are defined by points B_1 , B_2 , and B_3 (the position of point B_j on the j -th block is irrelevant since all blocks have purely translational motion). The positions of points P_i and B_j on plane $x-y$ and their displacements for a given motion are defined as follows:

$$\begin{aligned}\mathbf{p}_i &= P_i - O = \begin{bmatrix} x_{P_i} \\ y_{P_i} \end{bmatrix}, \quad \Delta\mathbf{p}_i = \begin{bmatrix} \Delta x_{P_i} \\ \Delta y_{P_i} \end{bmatrix}, \quad i \in \{1, \dots, 14\} \\ \mathbf{b}_j &= B_j - O = \begin{bmatrix} x_{B_j} \\ y_{B_j} \end{bmatrix}, \quad \Delta\mathbf{b}_j = \begin{bmatrix} \Delta x_{B_j} \\ \Delta y_{B_j} \end{bmatrix}, \quad j \in \{1, 2, 3\}\end{aligned}\tag{3}$$

We also define the displacement Δl_i of node N_i (along the belt direction at N_i) after a motion of the print head. The linear displacements Δl_i are assumed positive along the positive x or y axis (along the corresponding belt segment). We then write the constraint equations, which, after [37], can be categorized as follows:

- *Block-block constraints*: these equations are written as

$$\begin{aligned}\Delta x_{B_1} &= 0 \\ \Delta y_{B_1} &= 0 \\ \Delta x_{B_1} &= \Delta x_{B_2} \\ \Delta y_{B_2} &= \Delta y_{B_3}\end{aligned}\tag{4}$$

The first two equations of (4) correspond to fixing the frame position, while the remaining two correspond to the constraints introduced by the P_y and P_x joints, respectively. Notice that the two P_y joints in Figure 5 are redundant, as they both introduce the same constraint (namely, that the bar can only translate along the y axis with respect to the frame); using two joints is only convenient for design purposes, to reduce the stresses on the components and increase the motion accuracy. Thus, only one P_y joint is considered here without changing the DoFs of the mechanism.

- *Pulley-block constraints*: since the 14 pulleys are connected to the blocks by R joints, each removing two DoFs, 28 such equations are found, which can be written as

$$\begin{aligned}\Delta x_{P_i} &= \Delta x_{B_j} \\ \Delta y_{P_i} &= \Delta y_{B_j}\end{aligned}\tag{5}$$

corresponding to the i -th pulley being connected to the j -th block.

- *Belt-block constraints:* no such equations are present, as the routing has a closed-loop configuration and the belt is not directly attached to any block.
- *Belt-pulley constraints:* the displacement Δl_i of node N_i is related to the rotation $\Delta\theta_i$ of the pulley that immediately precedes the corresponding cable segment and to the rotation of the next pulley (moving along the belt in a counterclockwise sense). For instance, the following equations can be written for node N_1 :

$$\begin{aligned}\Delta l_1 &= \Delta y_{P_1} + r_1 \Delta\theta_1 \\ \Delta l_1 &= \Delta y_{P_2} + r_2 \Delta\theta_2\end{aligned}\quad (6)$$

The equations in (6) depend on the displacements of pulleys 1 and 2 along y since the belt segment at N_1 is parallel to the y axis; similar equations can be written for the segments parallel to the x axis (we refer the reader to [37] for details). A total of 28 equations can be written for the 14 belt segments.

These constraints can be put in matrix form. We, thus, obtain a system of 60 equations

$$\mathbf{A}\Delta = \mathbf{0} \quad (7)$$

in 62 unknowns, namely the displacements Δx_{B_j} , Δy_{B_j} , Δx_{P_i} , Δy_{P_i} , Δl_i and $\Delta\theta_i$ in vector Δ (matrix \mathbf{A} is not reported here, for brevity). This appears to indicate that the CoreH-bot mechanism has $62 - 60 = 2$ DoFs, but in fact, this is not the case. Indeed, we can transform Equation (7) as $\mathbf{U}\Delta = \mathbf{0}$, where the 62×60 matrix \mathbf{U} is the *reduced row echelon form* of \mathbf{A} . \mathbf{U} is obtained via symbolic Gauss–Jordan elimination, which is computationally easy in this case since \mathbf{A} is highly sparse. It is found that the last row of \mathbf{U} contains only zeros, thus, indicating that one of the constraint equations is linearly dependent on the others; this confirms that the routing has three independent DoFs, as observed in Section 2.1.

From \mathbf{U} , one can also derive the equations of motion of the routing. For this, it is convenient to order the columns in \mathbf{A} , such that the last three correspond to the entries in Δ that are chosen as inputs. Here, we choose as input variables the components Δx_{B_3} and Δy_{B_3} of the displacement of the print head: these are equal to Δx and Δy , respectively. The third input variable can be, for instance, the rotation $\Delta\theta_{13}$ of pulley 13 on the print head; this corresponds to the internal DoF of the mechanism, namely the belt rotation. We are interested in the rotations of the actuated pulleys as output variables; we finally obtain

$$\begin{bmatrix} \Delta\theta_1 \\ \Delta\theta_4 \\ \Delta\theta_8 \\ \Delta\theta_{11} \end{bmatrix} = \underbrace{\begin{bmatrix} -\frac{r_{13}}{r_1} & -\frac{1}{r_1} & -\frac{1}{r_1} \\ -\frac{r_{13}}{r_4} & -\frac{1}{r_4} & -\frac{3}{r_4} \\ -\frac{r_{13}}{r_8} & \frac{1}{r_8} & -\frac{3}{r_8} \\ -\frac{r_{13}}{r_{11}} & \frac{1}{r_{11}} & -\frac{1}{r_{11}} \end{bmatrix}}_{\mathbf{M}} \begin{bmatrix} \Delta\theta_{13} \\ \Delta x_{B_3} \\ \Delta y_{B_3} \end{bmatrix}. \quad (8)$$

Equation (8) defines the inverse position kinematics of the mechanism; the equation for the inverse velocity kinematics is obtained by differentiating Equation (8) with respect to t , giving

$$[\omega_1, \omega_4, \omega_8, \omega_{11}]^T = \mathbf{M} [\dot{\omega}_{13}, \dot{x}_{B_3}, \dot{y}_{B_3}]^T. \quad (9)$$

Obtaining the direct position kinematics is slightly more complex in this case with respect to the other belt routings, as matrix \mathbf{M} in Equation (8) is nonsquare, and thus, cannot be directly inverted. Algebraic manipulation of the equations provides

$$\begin{aligned}\Delta\theta_{13} &= (-3r_1\Delta\theta_1 + r_4\Delta\theta_4 + r_8\Delta\theta_8 - 3r_{11}\Delta\theta_{11}) / (4r_{13}) \\ \Delta x_{B_3} &= \frac{1}{2}(r_8\Delta\theta_8 - r_4\Delta\theta_4) = \frac{1}{2}(r_{11}\Delta\theta_{11} - r_1\Delta\theta_1) \\ \Delta y_{B_3} &= \frac{1}{2}(r_1\Delta\theta_1 - r_4\Delta\theta_4) = \frac{1}{2}(r_{11}\Delta\theta_{11} - r_8\Delta\theta_8)\end{aligned}\quad (10)$$

under the constraint on the inputs

$$r_1\Delta\theta_1 - r_4\Delta\theta_4 + r_8\Delta\theta_8 - r_{11}\Delta\theta_{11} = 0 \quad (11)$$

which corresponds to the condition that the total belt length remains constant.

From the results above, a special case can be found. If we control the motors such that

$$\begin{aligned} -r_4\Delta\theta_4 &= r_{11}\Delta\theta_{11} = \Delta u \\ -r_1\Delta\theta_1 &= r_8\Delta\theta_8 = \Delta v \end{aligned} \quad (12)$$

we find that Equation (11) is automatically satisfied. Moreover, Equation (10) simplify as

$$\Delta\theta_{13} = \frac{1}{r_{13}}(-\Delta u + \Delta v), \quad \begin{bmatrix} \Delta x_{B_3} \\ \Delta y_{B_3} \end{bmatrix} = \begin{bmatrix} \Delta x \\ \Delta y \end{bmatrix} = \mathbf{J} \begin{bmatrix} \Delta u \\ \Delta v \end{bmatrix} \quad (13)$$

with \mathbf{J} as defined in Equation (1). Under the assumption in Equation (12), it is also easy to show that

$$\dot{\mathbf{p}} = \begin{bmatrix} \dot{x} \\ \dot{y} \end{bmatrix} = -\mathbf{J} \begin{bmatrix} r_4\omega_4 \\ r_1\omega_1 \end{bmatrix} = \mathbf{J} \begin{bmatrix} r_{11}\omega_{11} \\ r_8\omega_8 \end{bmatrix} \quad (14)$$

We, thus, have a mechanism with the same Jacobian as the H-bot and the CoreXY; the control of the motors is still reasonably simple since it only requires computing two control signals (one for each of the 1–8 and 4–11 actuated pulley pairs). Differentiating Equation (14) provides

$$\ddot{\mathbf{p}} = \begin{bmatrix} \ddot{x} \\ \ddot{y} \end{bmatrix} = -\mathbf{J} \begin{bmatrix} r_4\alpha_4 \\ r_1\alpha_1 \end{bmatrix} = \mathbf{J} \begin{bmatrix} r_{11}\alpha_{11} \\ r_8\alpha_8 \end{bmatrix} \quad (15)$$

with $\alpha_i = d\omega_i/dt$. Thus, as in the other routings for purely translational motion [33,36], the relationship between the accelerations of the motors and the nozzle is defined by matrix \mathbf{J} , which does not depend on the position of the mechanism. Furthermore, Equations (14) and (15) can be easily inverted *analytically*, which significantly simplifies the kinematic analysis.

In a practical design, for simplicity, one may select all pulleys to have equal radii, namely $r_i = r$ for $i = 1, \dots, 14$. While not necessary for the mechanism operation, this would simplify maintenance and spare part management. Notice, however, that the pulleys will not be all identical; indeed, using a one-sided synchronous belt with the teeth inside the belt loop, as in the H-bot (see Section 1.2.1), it is found that pulleys 1, 4, 5, 7, 8, 11, 12 and 14 must be toothed, while the remaining ones are smooth.

We now compare the total lengths of the belts in the three designs considered here. For simplicity, we now assume that all pulleys in Figures 3–5 are identical and have radius r . Having assumed that all belt segments are aligned either with the x or the y axis, this induces some restrictions on the dimensions. For example, the distance between pulleys 5 and 7 in the CoreH-bot routing must be $4r$, since the segments which connect them (5–6 and 6–7) are horizontal. For ease of comparison, we assume that the three routings have footprints defined by the same width W and depth D along the x and y axis, respectively, (see Figure 6). We also define the distance d between the pulleys on the mobile bar, which is assumed to be the same in each routing. Moreover, we assume that the size of the print head is negligible with respect to the belt length. The print head position is defined by point P in Figure 6a–c; here, we take the origin of the coordinate axes at the center of pulley 1 for the three routings (on the lower left in each schematic in Figure 6). Finally, we consider a special architecture for the CoreXY (compare Figure 6b with Figure 4); we take the fixed pulleys 6 and 10 to be coaxial but on different planes. Pulleys 9 and 5 are also coaxial; pulleys 5 and 6 are on the same horizontal plane, and 9–10 are on another plane, parallel to the first one and below it (as seen from above). With this design, the belts in Figure 6b are on different planes and do not intersect, but the segments connecting pulleys 5–6 and 9–10 partially overlap. In the figure, we show the belt on the upper plane, with a dashed

line for clarity. This design does not change the kinematic properties of the CoreXY routing but simplifies its analysis, since in this case, all belt segments are aligned with one of the coordinate axes.

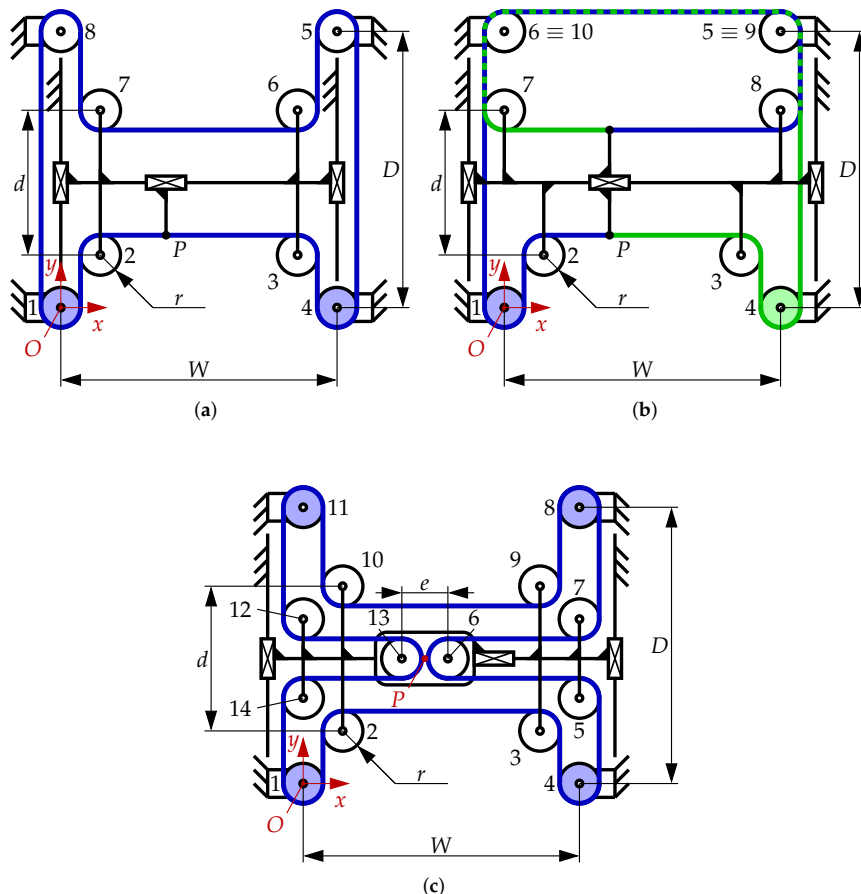


Figure 6. Comparison of the schematics of the three routings: (a) H-bot, (b) CoreXY, (c) CoreH-bot. Here, the CoreXY schematic (b) is simplified with respect to Figure 4: pulleys 6 and 9 coincide with pulleys 10 and 5, respectively, thus, the two belts partially overlap (over the dashed segments).

We now derive the total length of the belt for the three designs. We report the length of each segment in the CoreH-bot routing in Table 1. Here, we assumed that pulleys 6 and 13 are almost tangent (at point P); therefore, the distance e between their centers is $2r$. Summing the lengths of all belt segments in Table 1, we find that the total length is given by

Table 1. Length of each belt segment, for the CoreH-bot schematic in Figure 6c: the segment $i-j$ connects the i -th and the j -th pulley, while the segment $i-i$ wraps (for either 90° or 180°) on the i -th pulley.

Segment	Length	Segment	Length	Segment	Length
1–2	$y - \frac{d}{2}$	6–7	$W - x - r$	11–12	$D - y - 2r$
2–2	$\frac{\pi}{2}r$	7–7	$\frac{\pi}{2}r$	12–12	$\frac{\pi}{2}r$
2–3	$W - 4r$	7–8	$D - y - 2r$	12–13	$x - r$
3–3	$\frac{\pi}{2}r$	8–8	πr	13–13	πr
3–4	$y - \frac{d}{2}$	8–9	$D - y - \frac{d}{2}$	13–14	$x - r$
4–4	πr	9–9	$\frac{\pi}{2}r$	14–14	$\frac{\pi}{2}r$
4–5	$y - 2r$	9–10	$W - 4r$	14–1	$y - 2r$
5–5	$\frac{\pi}{2}r$	10–10	$\frac{\pi}{2}r$	1–1	πr
5–6	$W - x - r$	10–11	$D - y - \frac{d}{2}$		
6–6	πr	11–11	πr		

$$L_{tot} = 4W + 4D - 2d - 20r + 10\pi r. \quad (16)$$

For comparison, the length of the belt in the H-bot routing shown in Figure 6a is

$$L_{tot} = 2W + 4D - 2d - 8r + 6\pi r \quad (17)$$

while the two belts in the CoreXY routing (Figure 6b) both have length

$$L_{tot} = 2W + 2D - d - 2r + 3\pi r \quad (18)$$

(for brevity, we do not report the lengths of each belt segment for these routings).

As expected, the total belt length in each of Equations (16)–(18) is constant and independent of the print head coordinates x and y . Moreover, the CoreH-bot routing has a longer belt than the H-bot; for the CoreXY, each of the two belts is shorter than the belt used for the CoreH-bot, but the latter has a shorter total belt length. While a longer belt increases costs and can reduce stiffness, for the CoreH-bot, this was not found to be a significant shortcoming during the design of a practical prototype (see Section 4).

From these results, we define the *reachable workspace* (RW), namely, the set of positions for point P that are compatible with the physical limits of the mechanism. For all routings, it is found that the section of the workspace on the x - y plane is a rectangle defined by

$$\begin{aligned} x &\in [x_{min}, x_{max}] \\ y &\in [y_{min}, y_{max}]. \end{aligned} \quad (19)$$

The RW is defined by the condition that all belt segments must have a strictly positive length at each allowable position. We disregard other possible conditions that may restrict the workspace, such as the range of the P joints or the interference between rigid components in the routing, as these issues can be avoided in the design phase. From the results in Table 1, it is found that the RW of the CoreH-bot is given by

$$\begin{aligned} x &\in [r, W - r], \quad x_{max} - x_{min} = W - 2r \\ y &\in \left[\frac{d}{2}, D - \frac{d}{2}\right], \quad y_{max} - y_{min} = D - d. \end{aligned} \quad (20)$$

For comparison, the RW for both the H-bot and the CoreXY routings is given by

$$\begin{aligned} x &\in [2r, W - 2r], \quad x_{max} - x_{min} = W - 4r \\ y &\in [r, D - d + r], \quad y_{max} - y_{min} = D - d. \end{aligned} \quad (21)$$

It is, thus, found that the CoreH-bot has a slightly larger workspace area in the x - y plane (for a given footprint $W \times D$) with respect to the other routings. In a practical design, dimensions W and D will be much larger than r and d (which are not shown to scale in the figures, for clarity); thus, the projection of the RW in the horizontal plane almost coincides with the total footprint $W \times D$, as shown by Equation (20), if r and d are disregarded. This is unlike most parallel mechanisms, in which the RW is much smaller than the footprint due to interferences and joint limits. The fact that the RW is rectangular is also an advantage in the design phase; the RW of the print head with respect to the build platform (considering the z -axis motion applied to the platform in an XY head design) is a rectangular cuboid.

The transmission error may also be of interest; we, thus, consider the effect of errors $d\theta_i$ in the angular positions of the actuated pulleys on the positioning error $d\mathbf{p} = [dx, dy]^T$ of the print head. The errors in the positions of the actuators are due to inevitable limits on the accuracy of the control system; it appears reasonable to assume that these positioning errors have a known maximum absolute value, thus $|d\theta_i| \leq d\theta_{max}$ for all i . We then seek the maximum possible error on the print head position for errors on the actuator positions within the expected range; namely,

$$dp_{max} = \max_{\|d\theta\|_\infty \leq d\theta_{max}} \{\|d\mathbf{p}\|_2\} \quad (22)$$

where $\|\bullet\|_\infty$ and $\|\bullet\|_2$ are the Chebyshev and the Euclidean norms of (\bullet) , respectively, while $d\theta = [d\theta_1, d\theta_4, d\theta_8, d\theta_{11}]$ is the vector of actuator errors. The relationship between dp and $d\theta$ can be derived from Equation (10), considering infinitesimal displacements $d\theta_i$ and assuming $r_i = r$ for all i . We finally obtain

$$\begin{aligned} dx &= \frac{1}{4}(-rd\theta_1 - rd\theta_4 + rd\theta_8 + rd\theta_{11}) \\ dy &= \frac{1}{4}(+rd\theta_1 - rd\theta_4 - rd\theta_8 + rd\theta_{11}) \end{aligned} \quad (23)$$

under the constraint on the input errors, derived from Equation (11), that

$$rd\theta_1 - rd\theta_4 + rd\theta_8 - rd\theta_{11} = 0. \quad (24)$$

It can be proven, then, that

$$dp_{max} = d\theta_{max} \|r\mathbf{J}\|_{\infty,2} = rd\theta_{max} \quad (25)$$

using the induced matrix norm $\|\bullet\|_{\infty,2}$ from [49], which had similarly been introduced to model the effect of actuation errors in a purely translational, parallel mechanism actuated by flexible elements. Notice that the maximum error on the print head position is constant and depends neither on the actual position of the mechanisms nor on the workspace size. Therefore, the workspace can be fully utilized, as the accuracy is constant across the RW; also, the CoreH-bot routing can, thus, be easily scaled for larger prototypes.

3. Static and Dynamic Analysis

Let us now consider the forces acting in the three belt routings previously described, both at a given (static) position and during a general (dynamic) motion.

Under static conditions, only the belt preload T acts on the components: this preload, manually applied during the assembly (see details in Section 4), is necessary to ensure that the belt does not become slack. In our prototype, the preload was, thus, chosen to be large enough so that the belt tensions will always be strictly positive, but not too large to avoid unnecessarily increasing stresses, and thus, fatigue effects. For more details on the design of belt-and-pulley systems with synchronous belts, we refer the reader to [34].

Under dynamic conditions, on the other hand, there are different loads (besides the preload) acting in the routings; these are due to the torques applied on the actuated pulleys.

To study these forces, we make some preliminary simplifying assumptions, as follows:

- (A) The belt is always taut and each belt segment is aligned either with the x or the y axis (see Section 2.2, conditions I and II). Thus, the forces transmitted by the belt segments to the pulleys are all directed along either the x or the y axis.
- (B) Elastic and frictional effects between the pulleys and the belt may be disregarded, and the force transmission is entirely due to the coupling between their profiles.
- (C) Inertial torques on the pulleys and frictional torques in the R joints (between the pulleys and the blocks on which they are mounted) can similarly be disregarded; thus, for an idle pulley, the forces in the two belt segments attached to it are always equal. For actuated pulleys, if the motor applies a torque, the tensions on the two segments are different so that the pulley is in equilibrium.
- (D) Disregarding nonlinear force effects, the superposition principle applies; thus, we consider only two dynamic motions, namely, those along the x and the y axes, with the EE at a generic position. The results obtained will then be valid for a generic dynamic motion, and with the EE at any pose within the workspace, also considering that the Jacobian \mathbf{J} , as defined in Equation (1), is constant.
- (E) Under static conditions, the belt tension in each segment is constant and equal to T .

(F) Under dynamic conditions, the belt tension changes with respect to the preload T . Some belt segments are under higher tension, as they are “pulled” by the closest actuated pulley, which rotates in a direction such that the corresponding displacements Δl_i will be towards the said pulley. Other segments are instead “pushed” by an actuated pulley, such that the displacement Δl_i is away from said pulley; thus, the tension in these segments will be lower. We assume that the changes in tension for the pulled and pushed segments are all constant and equal to $+\Delta T$ and $-\Delta T$, respectively. Finally, some belt segments may be pushed and pulled at the same time; we assume that their tension does not change but remains equal to the preload T .

As an example, in Figure 7, we show a simplified overconstrained routing, with one DoF and two actuated pulleys. In Figure 7a, the mechanism is in static equilibrium, and all belt segments have a tension equal to the preload T . In Figure 7b, on the other hand, a dynamic condition is shown, in which point P (of which the position \mathbf{p} defines the configuration of the routing) moves leftwards with velocity $\dot{\mathbf{p}}$; the pulleys rotate simultaneously at the same speed $\omega_1 = \omega_2$. A force \mathbf{F}_e is applied, opposite to $\dot{\mathbf{p}}$: this could be due to inertial effects (if $\dot{\mathbf{p}}$ is not constant) or to friction. The tension in segment 1-P (from pulley 1 to P) increases by ΔT , the tension in segment 2-P decreases by ΔT , while in 1-2 the tension remains the same; we then have $\mathbf{F}_e = 2\Delta T$.

Among these simplifying assumptions, condition F is the strongest one. Admittedly, in a real system, the belt tension variation is more complex than in our model; this variation depends on the lengths of the toothed belt segments [34], thus, it also depends on the position of the EE. However, this approach greatly simplifies the force distribution analysis in the routing; the results obtained are confirmed by the known properties of the CoreXY and H-bot routings [10,20] and by experimental results on our prototype.

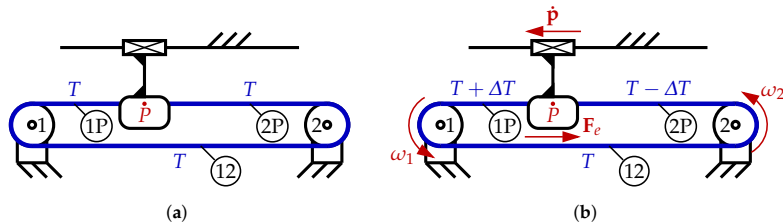


Figure 7. (a): Schematic of a simple, 1-DoF, overactuated belt routing, under static conditions. (b): The same, under dynamic conditions. Belt tensions are also shown for both conditions.

We now proceed to study the force transmission of the three routings in Figure 6. We consider the two mobile components (bar and print head) separately under static conditions: thus, all belt segments have the same tension T . Considering the CoreH-bot bar specifically, from Figure 8a, it is apparent that the total force acting on it is zero, as its components along the x and y axes are both given by $T + T + T + T - T - T - T - T = 0$; similarly, the x and y components of the force on the print head (Figure 8b) are both zero.

We define the torques τ_{B_2} and τ_{B_3} in the P joints (along the y and the x axis, respectively) with respect to the origin O of the coordinate system in Figure 6; torques are taken as positive in the counterclockwise direction. We also define the coordinates x_{P_i} and y_{P_i} of the center of the i -th pulley after the definitions in Section 2.2. From Figure 8a, we find

$$\begin{aligned} \tau_{B_2} - \tau_{B_3} &= -T(x_{P_2} - r) - T(y_{P_2} + r) - T(x_{P_{14}} - r) - T(y_{P_{14}} + r) \\ &\quad + T(x_{P_{10}} - r) - T(y_{P_{10}} - r) + T(x_{P_{12}} - r) - T(y_{P_{12}} - r) \\ &\quad + T(x_{P_9} + r) + T(y_{P_9} - r) + T(x_{P_7} + r) + T(y_{P_7} - r) \\ &\quad - T(x_{P_3} + r) + T(y_{P_3} + r) - T(x_{P_5} + r) + T(y_{P_5} + r) \\ &= T[(x_{P_{12}} - x_{P_{14}}) + (x_{P_{10}} - x_{P_2}) + (x_{P_9} - x_{P_3}) + (x_{P_7} - x_{P_5}) \\ &\quad + (y_{P_3} - y_{P_2}) + (y_{P_5} - y_{P_{14}}) + (y_{P_7} - y_{P_{12}}) + (y_{P_9} - y_{P_{10}})] \end{aligned} \quad (26)$$

and

$$\tau_{B_3} = T(y_{P_{13}} + r) + T(y_{P_{13}} - r) - T(y_{P_6} + r) - T(y_{P_6} - r) = 2T(y_{P_{13}} - y_{P_6}). \quad (27)$$

Here and in the following, we assume that all pulleys have the same radius r .

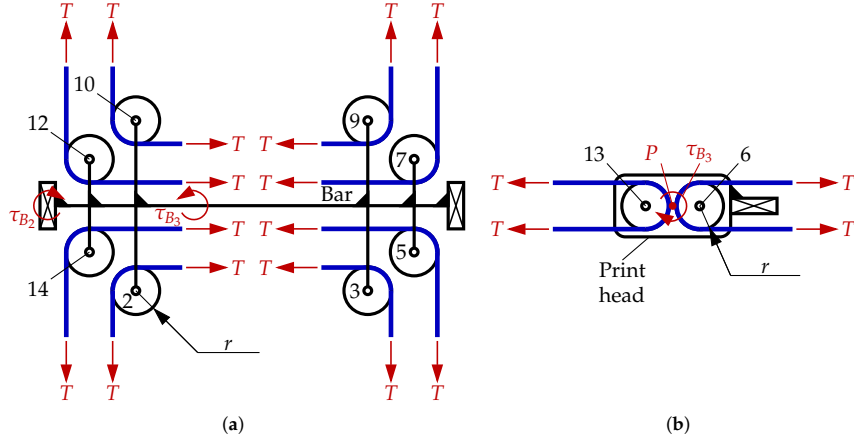


Figure 8. (a): Free-body diagram of the bar of the CoreH-bot, under static conditions; for clarity, the belt is “cut” in separate segments to illustrate the force distribution. (b): The same for the print head.

From Equation (27), we find that the torque τ_{B_3} is zero (and thus, in static conditions, no torque is applied to the horizontal P joint) if and only if $y_{P_{13}} = y_{P_6}$, that is, if the centers of pulleys 6 and 13 are horizontally aligned. Then, $\tau_{B_2} = 0$ (for the vertical P joints) holds if

$$x_{P_{12}} = x_{P_{14}}, \quad x_{P_{10}} = x_{P_2}, \quad x_{P_9} = x_{P_3}, \quad x_{P_7} = x_{P_5} \quad (28)$$

$$y_{P_3} = y_{P_2}, \quad y_{P_5} = y_{P_{14}}, \quad y_{P_7} = y_{P_{12}}, \quad y_{P_9} = y_{P_{10}}. \quad (29)$$

These constraints, which define the alignment of the mobile pulleys, are easily introduced in a practical design, thus, we applied them in our prototype; for simplicity of representation, the CoreH-bot schematics in this work show routings where the above constraints are respected. Similar constraints can also be found for the CoreXY and the H-bot.

We now consider dynamic motions along the coordinate axes, as shown in Figure 9. In the figure, each belt segment shows the sign of the corresponding change in tension. Thus, for instance, all segments denoted by “+” have tension $T + \Delta T$, while those denoted by “0” remain at the same tension T . An external force $\mathbf{F}_e = [F_{ex}, F_{ey}]^T$ acts to oppose the motion, such as in Figure 7b; the torques τ_i at the actuated pulleys have the same directions as the corresponding velocities ω_i . Applying hypothesis C, one can then find the τ_i . For instance, during a motion along the x axis, the torque applied by the belt on pulley 1 is $rT - r(T - \Delta T) = r\Delta T$ (in the counterclockwise sense), where the first and second term on the left-hand side are due to the tensions in segments 1–2 and 14–1, respectively. This torque is balanced by the motor torque τ_1 . By inspection of Figure 9a,b, it is found that in fact all torques have magnitude $r\Delta T$ for both motions shown.

From Equations (8) and (9) and the principle of kinematic-static duality [50], it is found that

$$\mathbf{W} = \mathbf{M}^T \boldsymbol{\tau} \quad (30)$$

in which $\mathbf{W} = [\tau_{13}, F_{ex}, F_{ey}]^T$ is the external wrench to be balanced, defined by the torque τ_{13} (acting on pulley 13) and the forces F_{ex} and F_{ey} (on the print head), while $\boldsymbol{\tau} = [\tau_1, \tau_4, \tau_8, \tau_{11}]^T$ is the vector of motor torques. For the components of the force \mathbf{F}_e , we find

$$F_{ex} = \frac{1}{r}(-\tau_1 - \tau_4 + \tau_8 + \tau_{11}) \quad (31)$$

$$F_{ey} = \frac{1}{r}(-\tau_1 - 3\tau_4 - 3\tau_8 - \tau_{11}). \quad (32)$$

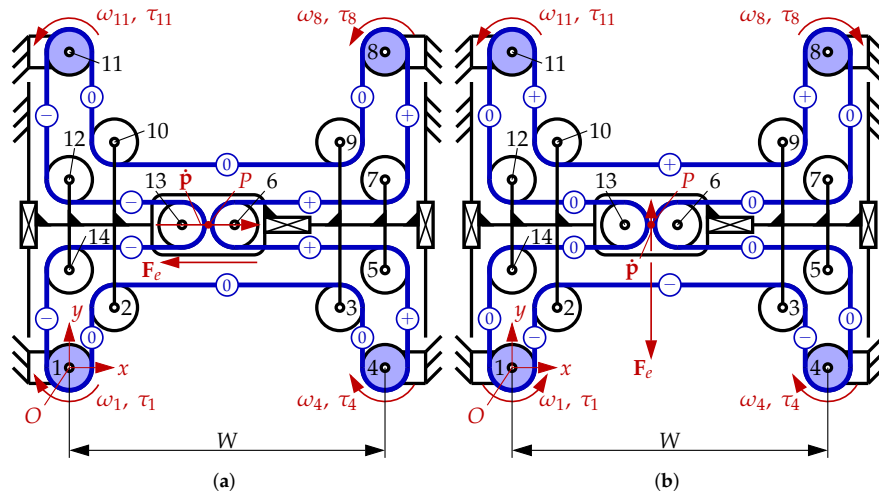


Figure 9. (a): Force distribution in the CoreH-bot, as the print head moves along the $+x$ direction. (b): The same for the $+y$ direction. The torques τ_i and angular speeds ω_i of the motors are also shown.

We can disregard τ_{13} , which, after hypothesis C, will be negligible in practical cases, since, during operation, no torque is applied on pulley 13.

Substituting $\tau_i = \pm r\Delta T$ (where the sign depends on the direction, as shown in Figure 9 in Equations (31) and (32)), it is found that, for a motion along the x -axis, one has $F_{ex} = 4\Delta T$ and $F_{ey} = 0$; for a motion along the y -axis, it holds $F_{ex} = 0$ and $F_{ey} = 4\Delta T$. Similarly, for both the H-bot and the CoreXY design, from Equation (1), one derives $\mathbf{F}_e = \frac{1}{r}\mathbf{J}^{-T}\boldsymbol{\tau}$, in which $\boldsymbol{\tau} = [\tau_1, \tau_4]^T$. However, the motor torques are not the same in all cases; thus, during a motion along the x -axis, it holds $\mathbf{F}_e = 2\Delta T$ for the H-bot, while for the Core-XY, it is $\mathbf{F}_e = 4\Delta T$. For both the H-bot and the Core-XY, it holds $\mathbf{F}_e = 4\Delta T$ during a motion along the y axis.

We now consider the torques acting under dynamic conditions. For the CoreH-bot, the torque τ_{B_3} in the P joint between the print head and the bar is zero, if $y_{P_{13}} = y_{P_6}$; similar conditions are derived for the other two routings. We are then interested in the torque τ_{B_2} between the bar and the lateral guides, which can damage the vertical P joints in the long run and causes a rotation of the bar, thus, reducing printing accuracy. We first compute the torque τ'_{B_2} due to the forces from the belt segments; the total torque τ_{B_2} is the sum of both τ'_{B_2} and the torques due to the other forces acting on the bar. Assuming that the conditions in Equations (28) and (29) are fulfilled, we can compute τ'_{B_2} during motion by considering only the torque terms due to the belt tension change ΔT ; the terms due to T , as reported in Equation (26), will cancel each other out. For motions along the x - and the y -axis, we find, respectively,

$$\begin{aligned} \tau'_{B_2} &= +\Delta T(x_{P_{14}} - r) + \Delta T(y_{P_{14}} + r) - \Delta T(x_{P_{12}} - r) + \Delta T(y_{P_{12}} - r) \\ &\quad + \Delta T(x_{P_7} + r) + \Delta T(y_{P_7} - r) - \Delta T(x_{P_5} + r) + \Delta T(y_{P_5} + r) \\ &= 2\Delta T(y_{P_5} + y_{P_7}) \end{aligned} \quad (33)$$

and

$$\begin{aligned}\tau'_{B_2} &= +\Delta T(x_{P_{10}} - r) - \Delta T(y_{P_{10}} - r) + \Delta T(x_{P_9} + r) + \Delta T(y_{P_9} - r) \\ &\quad + \Delta T(x_{P_3} + r) - \Delta T(y_{P_3} + r) + \Delta T(x_{P_2} - r) + \Delta T(y_{P_2} + r) \\ &= 2\Delta T(x_{P_2} + x_{P_3})\end{aligned}\quad (34)$$

where we simplified the results through Equations (28) and (29). For the x -axis motion in Figure 9a, the total torque τ_{B_2} is τ'_{B_2} plus the torque due to the reaction force in the guides. This force has magnitude $\mathbf{F}_e = 4\Delta T$ (but opposite orientation) and is distributed between the two vertical P joints, which introduces one redundant constraint along the x direction. Therefore, the actual force distribution in the P joints depends on the stiffness of the components; however, the total reaction force can be assumed as applied in the middle of the P joints, thus, its line of action passes through point P . Thus, we finally obtain

$$\tau_{B_2} = \tau'_{B_2} - \mathbf{F}_e \times \mathbf{p} = 2\Delta T(y_{P_5} + y_{P_7}) - 4\Delta Ty = 2\Delta T[(y_{P_5} + y_{P_7}) - 2y] \quad (35)$$

which is identically zero if

$$y = \frac{1}{2}(y_{P_5} + y_{P_7}) \quad (36)$$

namely, if the bar is symmetrical along its horizontal axis (and thus, $y_{P_5} = y - \frac{d}{2}$ and $y_{P_7} = y + \frac{d}{2}$). Again, this constraint is easily introduced in the design phase.

For the y -axis motion in Figure 9b, a force $-4\Delta T$ is applied by the print head to the bar through the horizontal P joint; this force, too, causes a torque on the bar, thus,

$$\tau_{B_2} = \tau'_{B_2} - \mathbf{F}_e \times \mathbf{p} = 2\Delta T(x_{P_2} + x_{P_3}) - 4\Delta Tx = 2\Delta T[(x_{P_2} + x_{P_3}) - 2x]. \quad (37)$$

For comparison, we also analyzed the other two routings; only the final results are presented here, for brevity. For the H-bot, the torque τ_{B_2} during a motion along the x axis is

$$\tau_{B_2} = -\Delta T[d + (x_{P_2} + x_{P_3})] \quad (38)$$

with d as defined in Section 2.2. On the other hand, under the same conditions, no torque is applied on the P joints for the CoreXY, if the condition in Equation (36) is fulfilled. For a motion along the y axis, all three routings develop the same torque, shown in Equation (37).

The torque in Equation (38) is *constant* and does not depend on the EE position; in this case, τ_{B_2} is close to $-\Delta T(x_{P_2} + x_{P_3}) = -\Delta T[2r + (L - 2r)] = -\Delta TW$ and is strictly larger than this value (we ignore the term proportional to d , which in a practical design will be small with respect to W). The torque in Equation (37), on the other hand, is *variable*: at a minimum, it is equal to zero when $x = \frac{1}{2}(x_{P_2} + x_{P_3}) = \frac{1}{2}W$, namely, when the EE is moving along the vertical axis of symmetry of the workspace. The maximum absolute value of the torque in Equation (37) is close to $2\Delta TW$, which is reached when the EE is moving close to the left or the right edge of the RW defined in Equation (20); notice that this torque will be in fact smaller than $2\Delta TW$, as it can be neither $x = 0$ nor $x = W$. In any case, these larger torque values are limited to extreme operation cases and can be avoided when positioning the components to be printed close to the center of the workspace if their dimensions are not too large.

In all three routings, the total torque due to all motors is zero for a motion along the y axis, as the motor torques cancel each other pairwise; for a motion along the x axis, the torque is (in absolute value) $2r\Delta T$ for the H-bot and $4r\Delta T$ for both the Core-XY and the Core-Hbot. This unbalanced torque is applied to the frame; while it does not directly influence the motion of the print head, it can cause vibrations if the printer frame has low stiffness, especially during highly dynamic operations (frequent in high-speed 3D printers), in which the direction of motion changes continuously.

To summarize, the dynamic behavior of the CoreH-bot is equivalent to that of the CoreXY, for all types of motion, and leads to a general reduction in the unbalanced torques applied to the prismatic joints with respect to the simpler H-bot design. It is well known [10]

that the torque τ_{B_2} causes a racking motion of the bar, thus, a degrading performance in the H-bot with respect to the CoreXY; our CoreH-bot design maintains the CoreXY advantages while keeping a fully planar structure, as discussed in Section 2.1.

Note that the control system could also be used to mitigate the unbalanced torques, as explored in [17]. However, the control design can only reduce (but not eliminate) unbalance effects on an intrinsically unbalanced mechanism. Moreover, advanced control strategies can also be applied to our CoreH-bot design to further improve performance.

4. CoreH-Bot: Our Prototype

A prototype has been developed in our laboratory to demonstrate the effectiveness of the concept proposed here. The design guidelines were to minimize the cost, size and corresponding printer footprint, while also guaranteeing ease of assembly and high dynamic performances. The workspace is a rectangular cuboid, as shown in Section 2.2. Its minimum dimensions are set as 300 mm × 300 mm × 300 mm.

The CAD model is shown in Figures 10 and 11. In our design, the P joints (on the lateral guides and on the moving bar) are precision ground bars (Figure 10a) on which linear bearings move with low friction. The belt has the “GT2” profile, commonly applied for 3D printers; this belt, made of polyurethane with tension members along its length, offers high stiffness and low friction coefficients, as the exterior is coated in PTFE [34].

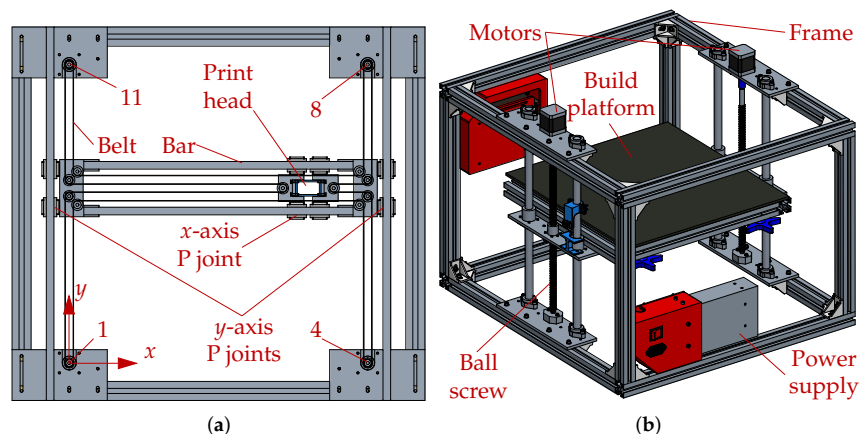


Figure 10. (a): The CoreH-bot belt routing, from our CAD model (section view from below). (b): The printer frame and the mechanism for z-axis motion; the belt routing is not shown here, for clarity.

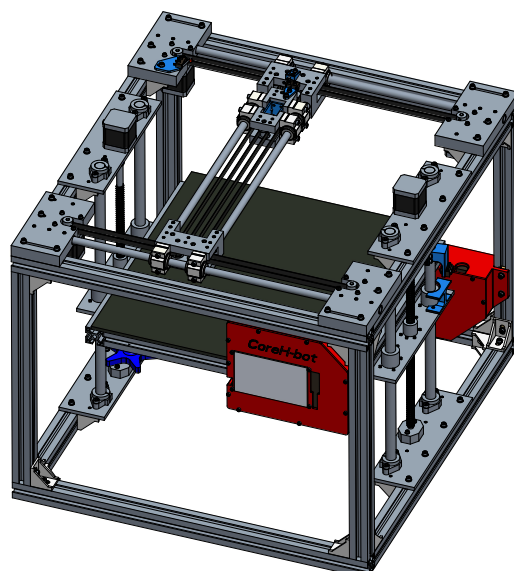


Figure 11. Top view (with the belt routing).

Unlike the CoreXY and the H-bot, our design has a closed belt loop. Thus, to apply the required preload T (Section 3), the motors, mounted on slots, can be moved laterally along the y axis (Figure 10a); this does not change the kinematic properties of the routing, but allows us to regulate the preload by hand during assembly. The belt also defines the workspace size. In our design, we take $W = D$ (see Table 2) for simplicity. Thus, from Equation (16), the belt length is approximately $8W$, disregarding the pulley radius $r \approx 6.3$ mm and the bar width $d = 52.4$ mm. From Equation (20), we need at least $W > 300$ mm to guarantee the required workspace. In the end, we opted for $W = 470$ mm and a belt having a length of ≈ 3600 mm.

Table 2. Main design parameters for the prototype.

Definition	Value
Width W (equal to depth D)	470 mm
Pulley radius r at pitch circle	6.35 mm
Distance d (pulleys on bar)	52.4 mm
Distance e (pulleys on head)	80 mm
Heated bed (print area size)	430 × 400 mm
Motion range (along z axis)	335 mm
Ball screw diameter and pitch	M12 × 4
Diameter of $x-y$ plane bars	12 mm
Total length of belt loop	3600 mm
GT2 belt pitch and height	2 × 9 mm
Frame profile (cross section)	30 × 30 mm

The actuated pulleys 1, 4, 8 and 11 are connected to stepper motors: these motors are commonly employed in commercial 3D printers as they are both cheap and accurate (especially when they have to maintain a given angular position) and allow us to use open-loop control. The relatively smaller torque of the stepper motors (as compared to servo motors) is not an issue here, since only small forces are applied. As discussed in Section 2, the motors are pairwise electronically coupled; differentiating Equation (12) with respect to time, we find $\omega_1 = -\omega_8$ and $\omega_4 = -\omega_{11}$, since the pulleys have the same radius r . This could be achieved by using only two motors, attached, for instance, to pulleys 1 and 4, to which the other actuated pulleys 8 and 11 are connected (respectively) through a mechanical transmission system, for instance, another belt and pulley drive. However, this approach would complicate the design and increase the size of the routing (in the direction of the z axis), which would no longer be fully planar. Given the low cost of stepper motors, it is in fact cheaper to install four separate motors, which are pairwise controlled by connecting them in series. Thus, motors 1 and 8 receive the same control signal, but with opposite phasing (motors 4 and 11 are similarly connected). This way, we can use a commercial controller board for 3D printers. As shown in Equation (14), our design is kinematically equivalent to a CoreXY routing, of which the control system is already implemented in commercially available control boards.

Applying the Cartesian XY head concept (Figure 2b), the CoreH-bot is fixed on top of a frame (in the shape of a rectangular cuboid) and provides the motion of the print head along the x and y horizontal axes. The z -axis motion is instead applied to the build platform, which is supported on its sides by two motorized ball screws (Figure 10b); this design is thus overconstrained, but offers better stiffness and accuracy. The platform is a commercial heated bed of size 430 mm × 400 mm to reduce thermal shock on the printed parts; its vertical position can also be fine-tuned with support springs that can be regulated by hand, to ensure a uniform distance from the nozzle while printing.

On the printer, a commercial filament extruder is mounted, having a motor that “pulls in” the filament to be melted. Mounting the extruder motor on the print head increases the moving inertia. While other designs with a frame-fixed motor exist (for instance, where the motor pushes the filament through a flexible tube), these latter have lower flexibility in terms of materials that can be used for printing, thus, we opted for a more standard design.

The other components in our design, which were not directly available on the market, were custom-made in Ergal, a lightweight, high-resistance aluminum alloy. The final prototype is shown in Figure 12. Since the CoreH-bot design has the same dynamic properties of the CoreXY, as shown in Section 3, it is expected that it will also provide similar performances in terms of speed and accuracy. Indeed, our simple prototype, designed exclusively for demonstration purposes with materials available in our laboratory, has been able to print at high speed while keeping an accuracy comparable to commercial desktop devices; the nozzle can deposit material with a speed of up to $250 \frac{\text{mm}}{\text{s}}$, comparable to that of similar prototypes [15] and of commercial 3D printers. Measurements with calipers indicate that the dimensional tolerance of the printed components is around 0.1 mm, which is comparable with that of standard desktop printers. The stepper motors we used have a maximum angular error $d\theta_{max} \approx 0.9^\circ$, which is half of the angular step. From Equation (25), we then obtain $dp_{max} \approx 0.099 \text{ mm}$, which is close to the dimensional tolerance. While other effects influence the print accuracy beyond error transmission, the results from both the tests and the theoretical model confirm that the design tolerances are adequate for the task. Further preliminary tests were also carried out, in which the print head moved (without printing) at up to $300 \frac{\text{mm}}{\text{s}}$ without issue. It is expected that, with further design optimization, higher speeds could be achieved, for instance, by reducing the moving weight and increasing the motor sizes. The total cost of the materials is $\approx 1500 \text{ €}$: while more expensive than mass-produced printers for the consumer market, this cost is comparable with similar prototypes [16,25] and could easily be reduced through a manufacturing-oriented redesign.

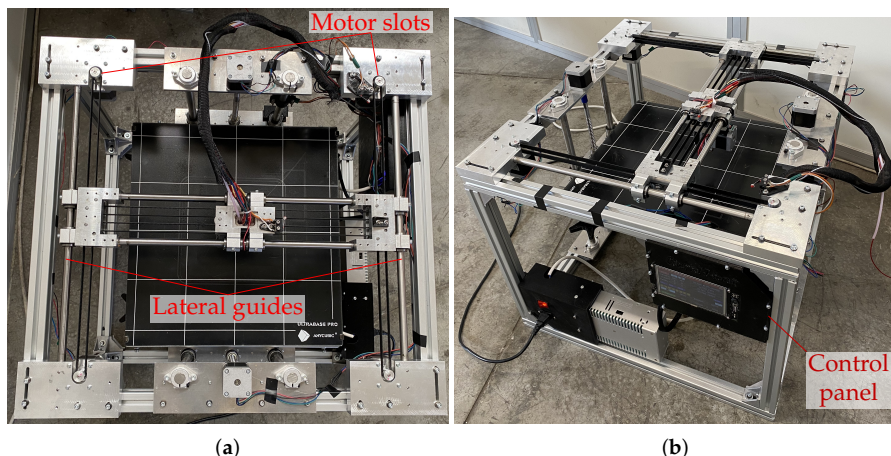


Figure 12. (a): Top view of our assembled prototype. (b): The same from a side view.

A video of the robot performing an example print is available in the multimedia attachment for this work (see video abstract attached to the paper). The accuracy of the prints was found to be comparable with that of high-end 3D printers available on the market.

5. Conclusions and Future Work

In this work, we presented a novel concept for a 3D printer, specifically for the xy -plane motion stage, which controls the print head movement through pulleys and synchronous belts. This concept, which we called CoreH-bot, combines attractive features of similar existing systems: it is both fully planar (and thus, compact) and partially balanced during motion, which reduces vibrations and increases printing accuracy. Therefore, the proposed concept has interesting advantages in comparison to both the H-bot routing, which has significant unbalanced torques, and to the CoreXY, which is not planar (and thus, more complex to design). To the best of our knowledge, no other 3D printer has been proposed with this concept. We analyzed the kinematic, static, and dynamic behavior of the CoreH-bot and compared it with known alternatives; a simple model allowed us to study the

unbalanced torques on the bar, showing that in this regard, the CoreH-bot is comparable to existing systems, while being more compact. We then developed a prototype to showcase the effectiveness of the concept: despite having been realized merely for demonstration purposes, and thus, being far from optimized, the prototype confirmed the theoretical results in printing tests.

Our goal is to use the prototype developed both to verify the feasibility of the CoreH-bot concept, with the aim of further industrial development and production for launch in the 3D printer market, and to quickly produce plastic components for our day-to-day needs in laboratory activities. The printer is currently under use in our lab at the University of Bologna for standard desktop 3D printing of plastic parts.

In future work, we aim to test the upper limits of the print-head speed on standard dynamic motions and to measure the printing accuracy on reference models. For instance, it would be interesting to compare the performance of our design with the 3-DoF printer in [51], which is also based on flexible elements (but has a different design concept), by printing the same reference models proposed therein and measuring the dimensional errors. Moreover, we will study the dynamics of the mechanism by taking the belt elasticity into account to provide a more complete model and to analyze the effect of using a longer belt. Finally, we aim to find the natural frequencies of the prototype, for instance, by a finite element analysis or through an experimental modal analysis, to verify whether resonance can be an issue during operation.

6. Patents

Parts of this work were patented in the following patent application: Idà, E.; Nanetti, F.; Zani, M.: *Dispositivo per la movimentazione di un organo estrusore di una macchina di manifattura additiva*. 20 October 2021, Italian Patent Application No. IT102021000026930.

Author Contributions: Conceptualization, F.N. and E.I.; methodology, F.N. and E.I.; software, G.M.; validation, F.N. and E.I.; formal analysis, E.I. and G.M.; investigation, F.N. and E.I.; resources, E.I.; writing—original draft preparation, G.M.; writing—review and editing, E.I. and G.M.; visualization, G.M.; supervision, E.I. and G.M.; project administration, E.I.; funding acquisition, E.I. All authors have read and agreed to the published version of the manuscript.

Funding: This research received no external funding.

Acknowledgments: The authors wish to thank Marco Zani and Mark One S.r.l. for their support in the development of the prototype.

Conflicts of Interest: The authors declare no conflict of interest.

References

1. Pham, D.T.; Gault, R.S. A comparison of rapid prototyping technologies. *Int. J. Mach. Tools Manuf.* **1998**, *38*, 1257–1287. [[CrossRef](#)]
2. Gibson, I.; Rosen, D.W.; Stucker, B.; Khorasani, M. *Additive Manufacturing Technologies*; Springer: Berlin/Heidelberg, Germany, 2021. [[CrossRef](#)]
3. Kodama, H. Automatic method for fabricating a three-dimensional plastic model with photo-hardening polymer. *Rev. Sci. Instrum.* **1981**, *52*, 1770–1773. [[CrossRef](#)]
4. Hull, C.W. Apparatus for Production of Three-Dimensional Objects by Stereolithography. United States Patent US4575330A, 11 March, 1986. Available online: <https://patents.google.com/patent/US4575330A/en> (accessed on 17 June 2022).
5. Standard EN ISO/ASTM 52900:2021; Additive Manufacturing—General Principles—Fundamentals and Vocabulary. International Organization for Standardization: Geneva, Switzerland, 2021. Available online: <https://www.iso.org/standard/74514.html> (accessed on 17 June 2022).
6. Wong, K.V.; Hernandez, A. A review of additive manufacturing. *Int. Sch. Res. Not.* **2012**, *2012*, 208760. [[CrossRef](#)]
7. Scott, J.; Gupta, N.; Weber, C.; Newsome, S.; Wohlers, T.; Caffrey, T. *Additive Manufacturing: Status and Opportunities*; Technical report; Science and Technology Policy Institute: Washington DC, USA, 2012. Available online: https://www.researchgate.net/profile/Justin-Scott-4/publication/312153354_Additive_Manufacturing_Status_and_Opportunities/links/59e786db458515c3630f917b/Additive-Manufacturing-Status-and-Opportunities.pdf (accessed on 17 June 2022).
8. Ngo, T.D.; Kashani, A.; Imbalzano, G.; Nguyen, K.T.Q.; Hui, D. Additive manufacturing (3D printing): A review of materials, methods, applications and challenges. *Compos. Part B Eng.* **2018**, *143*, 172–196. [[CrossRef](#)]

9. Crump, S.S. Apparatus and Method for Creating Three-Dimensional Objects. United States Patent US5121329A, 9 June 1992. Available online: <https://patents.google.com/patent/US5121329A/en> (accessed on 17 June 2022).
10. Shah, J.; Snider, B.; Clarke, T.; Kozutsky, S.; Lacki, M.; Hosseini, A. Large-scale 3D printers for additive manufacturing: Design considerations and challenges. *Int. J. Adv. Manuf. Technol.* **2019**, *104*, 3679–3693. [CrossRef]
11. Campana, G.; Mele, M.; Ciotti, M.; Rocchi, A. Environmental impacts of self-replicating three-dimensional printers. *Sustain. Mater. Technol.* **2021**, *30*, e00335. [CrossRef]
12. Ciotti, M.; Campana, G.; Mele, M. A review of the accuracy of thermoplastic polymeric parts fabricated by additive manufacturing. *Rapid Prototyp. J.* **2021**, *28*, 358–389. [CrossRef]
13. Ligon, S.C.; Liska, R.; Stampfl, J.; Gurr, M.; Mühlhaupt, R. Polymers for 3D printing and customized additive manufacturing. *Chem. Rev.* **2017**, *117*, 10212–10290. [CrossRef]
14. Turner, B.N.; Strong, R.; Gold, S.A. A review of melt extrusion additive manufacturing processes: I. Process design and modeling. *Rapid Prototyp. J.* **2014**, *20*, 192–204. [CrossRef]
15. Go, J.; Hart, A.J. Fast desktop-scale extrusion additive manufacturing. *Addit. Manuf.* **2017**, *18*, 276–284. [CrossRef]
16. Vasquez, J.; Twigg-Smith, H.; O’Leary, J.T.; Peek, N. Jubilee: An extensible machine for multi-tool fabrication. In Proceedings of the 2020 CHI Conference on Human Factors in Computing Systems, Honolulu, HI, USA, 25–30 April 2020; Association for Computing Machinery: Honolulu, HI, USA, 2020. [CrossRef]
17. Edoimoya, N.; Ramani, K.S.; Okwudire, C.E. Software compensation of undesirable racking motion of H-frame 3D printers using filtered B-splines. *Addit. Manuf.* **2021**, *47*, 102290. [CrossRef]
18. Weikert, S.; Ratnaweera, R.; Zirn, O.; Wegener, K. Modeling and measurement of H-Bot kinematic systems. In Proceedings of the 26th Annual Meeting American Society for Precision Engineering, Denver, CO, USA, 18 November 2011; ASPE: Denver, CO, USA, 2011. Available online: https://www.iwf.mavt.ethz.ch/ConfiguratorJM/publications/MODELING_A_132687166151936/3314_mod.pdf (accessed on 17 June 2022).
19. Comb, J.W.; Swanson, W.J.; Crotty, J.L. Gantry assembly for Use in Additive Manufacturing System. United States Patent US20130078073A1, 28 March 2013. Available online: <https://patents.google.com/patent/US20130078073A1/en> (accessed on 17 June 2022).
20. Peek, N.; Moyer, I. Popfab: A case for portable digital fabrication. In Proceedings of the 11th International Conference on Tangible, Embedded, and Embodied Interaction, Yokohama, Japan, 20–23 March 2017; Association for Computing Machinery: Yokohama, Japan, 2017; pp. 325–329. [CrossRef]
21. Avdeev, A.R.; Shvets, A.A.; Torubarov, I.S. Investigation of kinematics of 3D printer print head moving systems. In Proceedings of the 5th International Conference on Industrial Engineering (ICIE 2019), Sochi, Russia, 25–29 March 2019; Lect. Notes Mechanical Engineering; Springer: Berlin/Heidelberg, Germany, 2019; pp. 461–471. [CrossRef]
22. Clavel, R. ; Device for the Movement and Positioning of an Element in Space. United States Patent US4976582A, 11 December 1990. Available online: <https://patents.google.com/patent/US4976582A/en> (accessed on 17 June 2022).
23. Záda, V.; Belda, K. Structure design and solution of kinematics of robot manipulator for 3D concrete printing. *IEEE Trans. Autom. Sci. Eng.* **2022**. [CrossRef]
24. Furuya, N.; Makino, H. Research and development of selective compliance assembly robot arm (1st report)—Characteristics of the system. *J. Jpn. Soc. Precis. Eng.* **1980**, *46*, 1525–1531. [CrossRef]
25. Zhao, D.; Li, T.; Shen, B.; Jiang, Y.; Guo, W.; Gao, F. A multi-DOF rotary 3D printer: Machine design, performance analysis and process planning of curved layer fused deposition modeling (CLFDM). *Rapid Prototyp. J.* **2020**, *26*, 1079–1093. [CrossRef]
26. Urhal, P.; Weightman, A.; Diver, C.; Bartolo, P. Robot assisted additive manufacturing: A review. *Robot. Comput. Integrat. Manuf.* **2019**, *59*, 335–345. [CrossRef]
27. Vu, D.S.; Foucault, S.; Gosselin, C.; Kövecses, J. Design of a locomotion interface for gait simulation based on belt-driven parallel mechanisms. In Proceedings of the 2015 IEEE International Conference on Robotics and Automation (ICRA), Seattle, WA, USA, 26–30 May 2015; IEEE: Seattle, WA, USA, 2015; pp. 1581–1586. [CrossRef]
28. Vu, D.S.; Kövecses, J.; Gosselin, C. Trajectory planning and control of a belt-driven locomotion interface for flat terrain walking and stair climbing. In Proceedings of the 2017 IEEE World Haptics Conference (WHC), Munich, Germany, 6–9 June 2017; IEEE: Fürstenfeldbruck, Germany, 2017; pp. 189–194. [CrossRef]
29. Gosselin, C.; Laliberté, T. On the development of a walking rehabilitation device with a large workspace. In Proceedings of the IEEE 2011 ICORR, Zurich, Switzerland, 29 June–1 July 2011; IEEE: Zurich, Switzerland, 2011. [CrossRef]
30. Gosselin, C.; Laliberté, T.; Mayer-St-Onge, B.; Foucault, S.; Lecours, A.; Duchaine, V.; Paradis, N.; Gao, D.; Menassa, R. A friendly beast of burden—A human-assistive robot for handling large payloads. *IEEE Robot. Autom. Mag.* **2013**, *20*, 139–147. [CrossRef]
31. Forgó, Z.; Szilágyi, A. Dynamic modeling of new modular manipulators. In Proceedings of the 47st International Symposium on Robotics, Munich, Germany, 21–22 June 2016; IEEE: Munich, Germany, 2016; pp. 515–520. Available online: <https://ieeexplore.ieee.org/abstract/document/7559162> (accessed on 17 June 2022).
32. Forgó, Z.; Tolvaly-Roșca, F. Analytical and numerical model of low DOF manipulators. *Proc. Technol.* **2015**, *19*, 40–47. [CrossRef]
33. Zhu, J.; Li, B.; Mu, H.; Li, Q. Kinematic analysis of a flexible planar 2-DOF parallel manipulator. In *Lecture Notes in Computer Science, Proceedings of the International Conference on Intelligent Robotics and Applications (ICIRA 2019)*, Shenyang, China, 8–11 August 2019; Springer: Shenyang, China, 2019; Volume 11744, pp. 696–706. [CrossRef]

34. Perneder, R.; Osborne, I. *Handbook Timing Belts—Principles, Calculations, Applications*; Springer: Berlin/Heidelberg, Germany, 2012. [CrossRef]
35. Laliberté, T.; Gosselin, C.; Gao, D. Closed-loop transmission routings for Cartesian SCARA-type manipulators. In Proceedings of the ASME 2010 IDETC/CIE, Montreal, QC, Canada, 15–18 August 2010; ASME: Montreal, QC, Canada, 2010; Volume 2, pp. 281–290. [CrossRef]
36. Behzadipour, S. Kinematics and dynamics of a self-stressed Cartesian cable-driven mechanism. *J. Mech. Des.* **2009**, *131*, 061005. [CrossRef]
37. Hong, D.W.; Cipra, R.J. A method for representing the configuration and analyzing the motion of complex cable-pulley systems. *J. Mech. Des.* **2003**, *125*, 332–341. [CrossRef]
38. Webster, D.C. Recording Mechanism. United States Patent US2675291A, 13 April 1954. Available online: <https://patents.google.com/patent/US2675291A/en> (accessed on 17 June 2022).
39. Sollmann, K.S.; Jouaneh, M.K.; Lavender, D. Dynamic modeling of a two-axis, parallel, H-frame-type XY positioning system. *IEEE/ASME Trans. Mechatron.* **2009**, *15*, 280–290. [CrossRef]
40. Rice, Q. X-Y Workhead Positioning Device. Great Britain patent GB2274719A, 1994. Available online: <https://patents.google.com/patent/GB2274719A/en> (accessed on 17 June 2022).
41. Linhart, C.H. X-ray Apparatus Comprising a Film Cassette Which Is Displaceable in a Carrage. United States Patent US4961213A, 2 October 1990. Available online: <https://patents.google.com/patent/US4961213A/en> (accessed on 17 June 2022).
42. Kerschner, R.K. Differential Motor Drive for an XY Stage. United States Patent US6070480A, 2000. Available online: <https://patents.google.com/patent/US6070480A/en> (accessed on 17 June 2022).
43. Fustinoni, E. Apparatus for Laser Cutting and/or Marking. United States Patent US20070221621A1, 2007. Available online: <https://patents.google.com/patent/US20070221621A1/en> (accessed on 17 June 2022).
44. Etcheparre, J.; Etcheparre, B. Device for Driving and Displacing a Beam Resting Upon Guide Rails, and One or More Carriages Attached to the Beam. United States Patent US4315437A, 1982. Available online: <https://patents.google.com/patent/US4315437A/en> (accessed on 17 June 2022).
45. Budzyn, B.L. Chain Drive System for Mobile Loading Platform or for Two- or Three-Dimensional Indexing. United States Patent US3529481A, 1970. Available online: <https://patents.google.com/patent/US3529481A/en> (accessed on 17 June 2022).
46. Forgó, Z. Mathematical modelling of 4 DOF gantry type parallel manipulator. In Proceedings of the 41st International Symposium on Robotics and 6th German Conference on Robotics, Munich, Germany, 7–9 June 2010; IEEE: Munich, Germany, 2010; pp. 1206–1211. Available online: <https://ieeexplore.ieee.org/abstract/document/5756939> (accessed on 17 June 2022).
47. Harada, T. Novel Schönfliess motion parallel robot driven by differential mechanism. *Int. J. Mech. Eng. Robot. Res.* **2020**, *9*, 106–110. [CrossRef]
48. Chen, Y.; Squires, A.; Seifabadi, R.; Xu, S.; Agarwal, H.K.; Bernardo, M.; Pinto, P.A.; Choyke, P.; Wood, B.; Tse, Z.T.H. Robotic system for MRI-guided focal laser ablation in the prostate. *IEEE/ASME Trans. Mechatronics* **2017**, *22*, 107–114. [CrossRef] [PubMed]
49. Mottola, G.; Gosselin, C.; Carricato, M. Effect of actuation errors on a purely-translational spatial cable-driven parallel robot. In Proceedings of the 9th IEEE CYBER, Bengkulu, Indonesia, 22–23 September 2021; IEEE: Suzhou, China, 2019; pp. 701–707. [CrossRef]
50. Waldron, K.J.; Hunt, K.H. Series-parallel dualities in actively coordinated mechanisms. *Int. J. Robot. Res.* **1991**, *10*, 473–480. [CrossRef]
51. Zi, B.; Wang, N.; Qian, S.; Bao, K. Design, stiffness analysis and experimental study of a cable-driven parallel 3D printer. *Mech. Mach. Theory* **2019**, *132*, 207–222. [CrossRef]